https://doi.org/10.5194/egusphere-2025-5770
Preprint. Discussion started: 3 February 2026

Large-scale flood monitoring based on time series Sentinel-1 images and Z-index

Runmei Xing[1,2], Jun Zhao[1*]

[1] School of Civil Engineering, Zhengzhou University, Zhengzhou 450001, China
[2] Henan College of Transportation, Zhengzhou 451460, China

Correspondence to: Jun Zhao (zhaoj@zzu.edu.cn)

Abstract. Synthetic Aperture Radar (SAR) satellites have emerged as a crucial technology for real-time flood monitoring in the face of escalating flood disaster hazards. However, current flood extraction techniques still have a lot of drawbacks when it comes to solving the twin problems of accurate urban flood detection and extensive monitoring. To address this challenge, this study proposes a novel approach based on an analysis of backscatter characteristics across different land cover types, combined with multiple auxiliary datasets, enabling effective monitoring of both extensive flooding and inundation in building areas. First, an analysis of scattering behavior in time-series SAR images revealed that in natural areas, the consistency of backscatter intensity is strongly influenced by vegetation growth status. In urban areas, rainfall can intensify double-bounce scattering, also disrupting intensity consistency. Based on these findings, a Z-score-based flood classification tree was developed. This method uses reference images and flood-period images to compute Z-score maps, enabling pixel-level flood probability estimation and establishing flood detection thresholds with clear statistical significance. The integration of VV and VH polarizations within the classification tree further improves the reliability of flood identification. Applied to the 2021 Weihui flood event, the method demonstrated strong performance, achieving a critical success index (CSI) of 60% and overall accuracy (OA) of 90% in natural areas, and a CSI of 62% and OA of 73% in building areas. The proposed approach shows significant advantages in accurately classifying flood-affected areas and offers the capability to monitor both large-scale floods and urban inundation.

1 Introductions

Flooding is one of the most frequent, widespread, and economically devastating natural disasters worldwide (Jongman et al., 2012; Barredo, 2007; Tingsanchali, 2012). Statistics show that between 2000 and 2019, more than 1.6 billion people globally were affected by floods to varying degrees, with Asia alone accounting for 1.5 billion of those cases (Tellman et al., 2021). As global climate change intensifies, extreme weather events are becoming more frequent, and both the occurrence and severity of floods are on the rise. Satellite-based studies indicate that from 2000 to 2015, the proportion of the global population affected by floods increased by more than 20% (Voigt et al., 2016). It is projected that by 2030, the proportion of people affected by flooding in Asia and Africa will continue to increase (Voigt et al., 2016).

https://doi.org/10.5194/egusphere-2025-5770
Preprint. Discussion started: 3 February 2026

Extreme rainfall is the primary driver of widespread flooding (Kunkel, 2003). However, due to cloud cover, traditional optical and infrared remote sensing satellites often struggle to capture the actual conditions on the ground, making it difficult to promptly map the full extent of flood events and frequently leading to underestimation of the resulting damage (Anusha and Bharathi, 2020; Zhang et al., 2002; Alvarez-Vanhard et al., 2021). In contrast, synthetic aperture radar (SAR) is an active microwave sensing technology (Moreira et al., 2013; Cruz et al., 2022), enabling it to acquire surface information under all weather conditions and providing all-day, all-weather imaging capabilities (Cruz et al., 2022; Liu et al., 2025). Synthetic Aperture Radar satellites are a key component of the global Earth observation satellite system and play an indispensable role in flood emergency response. The European Space Agency's Sentinel-1, for instance, was deployed shortly after launch to support emergency response during flood events in Namibia and Bosnia and Herzegovina (Nhangumbe et al., 2023; Twele et al., 2016; Martinis et al., 2018). Similarly, China's Gaofen-3 captured multiple emergency images during the catastrophic "7•20" Zhengzhou rainstorm. These cases demonstrate that SAR has become one of the preferred tools for flood monitoring (Kang et al., 2018; Zhao et al., 2021; Wang et al., 2025). Moreover, the rapid development of commercial SAR satellites has introduced data with varying spatial resolutions, frequency bands, and polarization modes, significantly enhancing SAR's ability to map dynamic surface changes during emergency responses (Zhao et al., 2021; Martinis et al., 2015; Amitrano et al., 2024).

The timeliness and accuracy of flood mapping are critical for the effective allocation of rescue resources and the reduction of casualties. In natural areas, floods are generally easy to identify using SAR images, as the smooth surface of water causes strong specular reflection, leading to a significant decrease in backscatter values (Tripathi et al., 2020). Medium-resolution SAR (MR-SAR) images is often sufficient for effective monitoring in such cases. However, in urban areas, the scattering characteristics are more complex. Backscatter values are influenced by factors such as the satellite's orbit (ascending or descending), polarization mode, and the orientation and distribution of buildings (Wang and Tong, 2018). As a result, high-resolution SAR images is typically required for effective flood detection in urban environments (Cian et al., 2018; Voigt et al., 2009). The wide variability in the scale of flood disasters poses additional challenges for monitoring methods and technologies. Although high-resolution SAR images provides greater detail, its narrower swath limits its use in large-scale flood monitoring (Liu et al., 2020). At the same time, traditional MR-SAR image monitoring methods may exhibit significant errors in densely populated urban areas, leading to more severe consequences. Therefore, it is of great significance to develop methods that can support both large-scale monitoring and the detection of urban flooding simultaneously.

To address this issue, two approaches exist. The first involves expanding the coverage of high-resolution SAR imagery, but this depends on satellite availability and scheduling, making it difficult to achieve at present. Therefore, we opted for the second approach: optimizing methods based on MR-SAR imagery to ensure rapid, large-scale flood monitoring and effective detection of urban flooding in built-up areas. This study integrates the characteristics of SAR backscatter with time-series anomaly detection concepts to improve both the accuracy and timeliness of inundation detection in urban environments. To address the challenges posed by complex surface cover types and high heterogeneity in urban areas, this study analyzes the scattering mechanisms in building regions based on variations in microwave scattering features. Recognizing the distinct flood response behaviors in natural and urban areas, we propose a time series SAR-based anomaly flood monitoring method. By incorporating auxiliary data and dual-polarization SAR information, this approach achieves high robustness and accuracy in flood detection across both natural and urban environments.

2 Study area and data

2.1 Study area

Weihui City is located in the northern part of Henan Province, China, covering a total area of 862 km^2, with a north-south length of 43 km and an east-west width of 35 km (Fig. 1). Situated within the Hai River Basin, the city lies at the confluence of multiple rivers, including the Wei River and the Communism Canal, resulting in a large surface water area. The urban area is built on a plain formed by river sedimentation, featuring low-lying terrain that slopes from east to west, which hinders effective drainage of accumulated water. In recent years, rapid urbanization has altered the characteristics of the underlying surface, further increasing the risk of urban waterlogging. Climatically, Weihui experiences a temperate continental monsoon climate, characterized by hot and rainy summers. From July to August, precipitation accounts for approximately 50% of the annual total, often concentrated in a few intense rainstorms. Moreover, interannual variation in precipitation is significant—wet years may see rainfall as high as 1000 mm, while dry years may receive only 400 mm, a difference of more than 2.5 times. This results in highly variable river flows within the city, making summer the peak season for flood disasters in Weihui (Du et al., 2024; Zhang et al., 2022).

Starting on July 17, 2021, persistent heavy rainfall triggered widespread flooding across many parts of Henan Province. Records from the Xinxiang Meteorological Station indicated that this extraordinary rainstorm was the most intense since observations began, with a maximum recorded rainfall of 965.5 mm. Located downstream, Weihui City faced enormous pressure from upstream flood discharge even after the rainfall had ceased. River water levels continued to rise, eventually surpassing the warning thresholds. Overflows from the Wei River and the Communism Canal caused massive volumes of floodwater to inundate the urban area of Weihui, leading to extremely severe urban flooding. At its peak, 79% of the city's building area was submerged, with floodwater volume reaching 21,000,000 m^3. All four reservoirs in the city overflowed, making it impossible to discharge floodwaters via the river system. Compounding the issue, the city's power supply was disrupted by the flood, preventing pumping stations from operating at full capacity. As a result, floodwaters in the main urban area were not fully drained until July 31. Nearly 300,000 people were affected, and over 14,000 houses were inundated. In addition to the urban devastation, all 13 townships under Weihui's jurisdiction experienced varying degrees of flooding, with approximately 330 km^2 of crops damaged (Zhang et al., 2022).

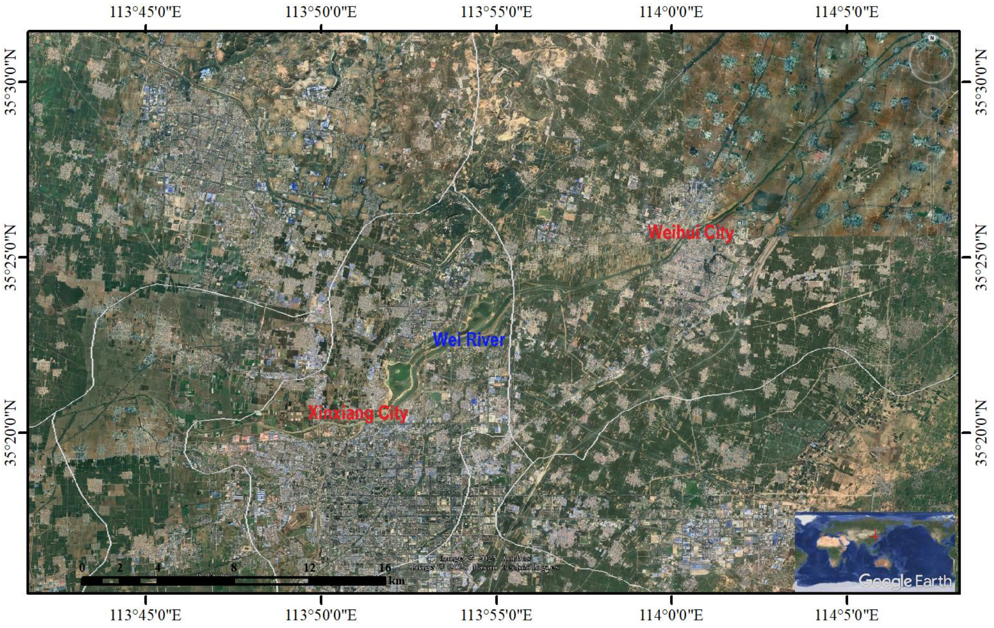

Figure 1: The geographical location of the study area. Imagery © 2022 NASA, Map data © 2022 Google

2.2 Sentinel-1 data

The Sentinel-1 satellite constellation currently consists of three satellites: Sentinel-1A, launched in 2014; Sentinel-1B, launched in 2016; and Sentinel-1C, launched in 2024. Sentinel-1B was officially decommissioned in August 2022 due to an irreparable power failure (Torres et al., 2012; Geudtner et al., 2014). When operating with a single satellite, Sentinel-1 has a revisit cycle of 12 days, with observation frequency reaching up to 6 days in certain regions (Torres et al., 2012). To meet diverse application needs, Sentinel-1 is equipped with four imaging modes: stripmap mode (SM), interferometric wide swath mode (IW), extra wide swath mode (EW), and wave mode (WV). Among these, the IW mode is the primary mode for land surface observation. It enables coverage of the vast majority of the Earth's land areas, with each acquisition providing a swath width of 250 km and a spatial resolution of 5×20 m.

This study primarily utilizes the intensity data from Sentinel-1 ground range detected (GRD) products for flood extraction (Nhangumbe et al., 2023; Torres et al., 2012). The data processing involves the following key steps: (1) Precise orbit correction – applying refined satellite orbit data to improve geolocation accuracy. (2) Thermal noise removal – eliminating sensor-induced noise to enhance image quality. (3) Radiometric calibration (*Sigma0*) – converting pixel values into physically meaningful backscatter intensity using the sensor calibration metadata embedded in the images. (4) Speckle filtering – applying Refined Lee filtering to reduce speckle noise while preserving image details. (5) Terrain correction – using a digital elevation model (DEM) to correct the influence of surface topography on backscatter intensity, resulting in a normalized backscatter coefficient. (6) Conversion to decibel scale (dB) – transforming the backscatter coefficient into logarithmic scale to facilitate easier computation and statistical analysis, especially for values that span several orders of magnitude.

The Sentinel-1 images used in this study corresponds to Path 40 (112) and Frame 113 (111), covering the period from January 4, 2021, to December 30, 2021. The flood event occurred in mid-to-late July, with large-scale floodwaters receding approximately by mid-to-late August.

2.3 GPM data

The global precipitation measurement (GPM) mission, developed through international collaboration among multiple space agencies, enables frequent and high-accuracy global precipitation observations. The satellite is equipped with two main instruments for precipitation monitoring: the dual-frequency precipitation radar (DPR) and the GPM microwave imager (GMI). The integrated multi-satellite retrievals for GPM (IMERG) precipitation product, provided by the National Aeronautics and Space Administration (NASA), is one of the key datasets derived from GPM observations (Tang et al., 2020). This product is primarily generated using GPM satellite data and is supplemented with data from other meteorological satellites, including TRMM, METOP, and NOAA (Kummerow et al., 2000). By integrating observations across various frequency bands and resolutions, the IMERG product enhances both the accuracy and spatiotemporal resolution of precipitation estimates. It offers global precipitation data at a temporal resolution of 30 minutes and a spatial resolution of 0.1°. In this study, the “precipitationCal” band from the IMERG product is used as the reference source for precipitation data. This band has been calibrated using ground-based observation station data and is the officially recommended product in the IMERG user manual. GPM data is mainly used to characterize rainfall intensity during the flood event and to assist in validating the flood extraction results.

2.4 Auxiliary data

The global surface water (GSW) dataset is a 30 m resolution product that provides global surface water distribution information spanning the past 38 years (Pekel et al., 2016). It is developed and continuously updated by the joint research center (JRC). Each pixel is classified as either water or non-water using an expert system, and then temporal analysis is applied to capture the historical dynamics of surface water presence. The algorithm proposed in this study uses the “occurrence” band from the GSW dataset, which represents the frequency of water occurrence for each pixel, with values ranging from 0 to 100%. Based on threshold values, surface water can be categorized into permanent water, seasonal water, and historic flood water. The DEM data used in this study is derived from the European Space Agency's Copernicus DEM, with a spatial resolution of 30 m (Li et al., 2022).

3 Methods

This study first uses a year-long, same-orbit Sentinel-1 time series to test the normality of pixel-wise backscatter (via skewness and kurtosis). VV and VH images are then standardized by the mean and standard deviation to produce Z-score anomaly maps, with thresholds set considering acquisition differences. To avoid missing persistently inundated areas, GSW water-occurrence frequency is used to mask seasonal/permanent water. A decision-tree classifier assigns flood labels in natural and urban areas using separate thresholds, distinguishing dual- or single-polarization floods. Finally, speckle-induced artifacts are removed by post-processing (e.g., small-patch filtering), and the results are validated with Sentinel-2/UAV imagery and assessed using binary metrics.

3.1 Outlier detection

Z-score is a statistical anomaly detection method that has been proven effective for monitoring newly formed surface water bodies. Compared to other anomaly detection approaches, Z-score relies on commonly used statistical measures—mean and standard deviation (std)—which offer strong interpretability. Thresholds can be defined based on the desired confidence level, providing solid theoretical support for better understanding the data and results (Fernandez et al., 2016; Cheadle et al., 2003). The Z-score method standardizes data using the mean and std, and it assumes that the data follow a normal distribution. If the data deviate significantly from normality, the reliability of the Z-score results may be compromised. Experiments conducted by DeVries et al. in various study areas demonstrated that backscatter characteristics of natural areas during the same season can generally be considered normally distributed, and their water body monitoring based on the Z-score method achieved an overall accuracy of 90% (DeVries et al., 2020). To verify whether the backscatter intensity of urban areas in time-series SAR images follows a normal distribution, this section employs kurtosis and skewness as statistical indicators.

Kurtosis is a statistical measure used to describe the shape of a data distribution. It indicates the degree to which a dataset contains outliers and tail risk. A normal distribution has a kurtosis value of 3. When subtracting 3 as a constant, the result is known as excess kurtosis, which equals 0 for a perfectly normal distribution. The formula for calculating excess kurtosis is (DeCarlo, 1997):

$$\text{Kurtosis} = \frac{n(n+1)\sum(x_i-\mu)^4}{(n-1)(n-2)(n-3)\sigma^4} - \frac{3(n-1)^2}{(n-2)(n-3)} - 3 \tag{1}$$

where x_i represents the elements in the array and n is the sample size, while μ and σ denote the mean and standard deviation of the array, respectively. The sign of the excess kurtosis indicates whether the shape of the distribution is sharper or flatter compared to a normal distribution. A positive excess kurtosis suggests a distribution with heavier tails and a higher likelihood of outliers, whereas a negative excess kurtosis indicates fewer outliers and a flatter distribution.

Skewness is a statistical measure that quantifies the degree of asymmetry in a data distribution. For example, a normal distribution has a skewness value of 0. In cases of asymmetric distributions, if the tail is longer on the left side, it is referred to as left-skewed (negative skewness); if the tail is longer on the right, it is right-skewed (positive skewness). Skewness is calculated by summing the cubed deviations from the mean and normalizing by the standard deviation. The formula for skewness is (Groeneveld and Meeden, 1984) :

$$\text{Skewness} = \frac{1}{n} \times \frac{\sum_{i=1}^{N} (x_i - \mu)^3}{\sigma^3} \tag{2}$$

where x_i represents the elements in the array and n is the sample size, while μ and σ denote the mean and standard deviation of the array, respectively. Skewness can be either positive or negative: right-skewed data has positive skewness, while left-skewed data has negative skewness. Skewness can be used to assess whether a dataset follows a normal distribution or another specific distribution, thereby providing a basis for statistical analysis or modeling.

This study selected long time-series Sentinel-1 images with consistent orbit numbers, covering an entire year (N images), to verify whether the temporal backscatter intensity follows a normal distribution. By calculating the kurtosis and skewness of this dataset, it is possible to assess whether the data conforms to a normal distribution. However, in practice, even if the data does follow a normal distribution, the calculated skewness may exhibit randomness due to the sample size. Additionally, the larger the number of sampled points, the more likely the values of kurtosis and skewness will be close to zero.

On the effect of sample size on skewness in normally distributed data, Doane et al. provided skewness coefficient thresholds corresponding to a 90% confidence level. Specifically, when the sample size is 40, the skewness should fall within the range of -0.594 to 0.594 (Doane, 2011). After obtaining the mean and standard deviation of the time-series SAR images, the Z-score values—accounting for differences in polarization mode, orbit parameters, and imaging mode—were calculated using the following formula:

$$Z_{flood}^{pq,o,m} = \frac{\sigma_{flood}^{pq,o,m} - mean(\sigma^{pq,o,m})}{std(\sigma^{pq,o,m})} \tag{3}$$

where Z represents the Z-score value, pq denotes the polarization mode (VV or VH), o indicates the orbit number, and m refers to the imaging mode. σ is the normalized backscatter coefficient, while *mean* and *std* refer to the mean and standard deviation calculations, respectively. Using a Z-score lookup table, the Z-score can be converted into a confidence level indicating the likelihood that a pixel is affected by flooding. For example, when the p-value is less than 0.05, the null hypothesis can be rejected, indicating a significant difference between the two data sets. This means that if the Z-score exceeds 1.96, there is a 95% confidence level that the observed difference is caused by flooding.

3.2 Flood monitoring classification tree

Using single-polarization SAR imagery alone yields limited accuracy in flood monitoring. Therefore, this study incorporates both VV and VH polarizations to provide multi-dimensional observational information and enhance the reliability of the flood mapping results. For example, during periods of heavy rainfall, rain and strong winds can increase water surface roughness, potentially leading to Bragg scattering dominance. This can strengthen the backscatter in co-polarized channels and obscure the presence of water bodies. In such cases, cross-polarization is less affected by surface roughness, offering additional evidence for flood delineation (Clement et al., 2018). In natural areas, the baseline images used in this study was acquired 2–3 months prior to the flood event. If certain regions were continuously covered by water during this period, anomaly detection methods would struggle to identify them as flooded. To address this, auxiliary permanent surface water data from the GSW v1.4 dataset was incorporated to ensure the accuracy of flood extent delineation (Pekel et al., 2016) . This section adopts the conceptual framework of decision tree classification, and by simultaneously considering dual-polarization information and surface water data, proposes a novel flood monitoring classification tree.

In this study, Equation (3) was applied pixel by pixel to both VV and VH images to generate their respective Z-score maps. The classification tree algorithm begins by determining the land cover type of each pixel. In natural areas, the first step is to identify whether a pixel represents a seasonal water body based on its water occurrence frequency. Typically, a pixel is classified as a seasonal water body if its “occurrence” value exceeds 25, meaning the pixel is identified as water in more than 25% of the annual satellite observations. Such pixels are labeled in blue and excluded from further classification. For non-seasonal water bodies, if both the VV and VH Z-score values of a given pixel fall below a predefined threshold (th_n), the pixel is assigned a dual-polarization flood label. If only one of the polarizations falls below the threshold (th_n), the pixel is assigned a single-polarization flood label. In urban (building) areas, flood labels are similarly assigned based on whether the Z-score values of VV and VH are below a separate threshold (th_s). The same rule-based logic is applied to determine single- or dual-polarization flood classifications. It is important to note that in urban areas, the color coding for flood labels differs from that used in natural areas.

In SAR-based flood monitoring, even when filtering algorithms are applied during the preprocessing stage, speckle noise cannot be completely eliminated. As a result, the final flood mapping output often contains scattered misclassified pixels within large, homogeneous land cover areas. These fragmented misclassifications negatively impact the overall accuracy and may reduce the reliability of the flood monitoring results. To address this issue, this study adopts a method known as pixel aggregation. This technique specifically targets small misclassified regions. In particular, if a flood-classified area consists of four or fewer connected pixels, these pixels are reclassified as non-flood. The goal is to minimize the impact of noise-induced misclassification and improve the overall classification accuracy. This step serves as a post-processing refinement of the threshold-based classification results. Other commonly used post-processing methods include morphological operations such as erosion and dilation based on opening and closing. Through such post-processing techniques, small fragmented errors can be effectively removed, thereby enhancing the accuracy of flood monitoring outcomes (Borrelli et al., 2020).

3.3 Accuracy verification of flood extraction

In this study, Sentinel-2 optical images and high-spatial-resolution unmanned aerial vehicle (UAV) optical images were used as validation data sources for flood extraction results in natural areas and urban (building) areas, respectively. The time difference between the Sentinel-2 images and the corresponding Sentinel-1 acquisition was 8–9 hours, while the UAV images had a 2-hour time difference. For water body extraction, the modified normalized difference water index (MNDWI) utilizes the green and short-wave infrared (SWIR) bands, which enhances the contrast between building areas and water bodies. This reduces confusion between the two and improves classification accuracy. The expression is as follows (Xu, 2006):

$$\mathrm{MNDWI} = \frac{\mathrm{Green} - \mathrm{SWIR}}{\mathrm{Green} + \mathrm{SWIR}} \tag{4}$$

where, in the Sentinel-2 images, the Green and SWIR bands correspond to Band-3 and Band-11, respectively. Since MNDWI is a normalized index, it also performs well in detecting water bodies located in shadowed areas.

In this study, high-confidence and medium-confidence flood pixels are both classified as flood pixels during accuracy assessment. Therefore, binary classification metrics are used for evaluation. The confusion matrix for binary classification is a 2×2 matrix, with the four elements being: True Positive (TP), True Negative (TN), False Positive (FP), and False Negative (FN). Common evaluation metrics based on these four elements include: overall accuracy (OA), user accuracy (UA), and producer Accuracy (PA). In flood monitoring, the flood class requires special attention, and prediction accuracy may not always be the primary concern—particularly in cases where class distribution is highly imbalanced. The critical success index (CSI), which considers both PA and UA, is a more suitable metric for flood monitoring as it effectively reflects both the accuracy and stability of predictions. Therefore, this study adopts four evaluation metrics, including CSI. Their formulas are as follows:

$$PA = \frac{TP}{TP + FN} \tag{5}$$

$$UA = \frac{TP}{TP + FP} \tag{6}$$

$$OA = \frac{TP + TN}{TP + FP + FN + TN} \tag{7}$$

$$CSI = \frac{TP}{TP + FP + FN} \tag{8}$$

4 Results and discussions

4.1 Scattering characteristics of natural areas and building areas in time-series SAR images

4.1.1 Natural areas

In this study, natural areas refer to regions with land cover types such as water bodies, bare soil, cropland, and forests—i.e., non-artificial surfaces. These areas exhibit different dominant scattering mechanisms in SAR images. For water-covered areas, the dominant scattering mechanism is specular reflection. However, ripples or waves caused by wind or other

https://doi.org/10.5194/egusphere-2025-5770
Preprint. Discussion started: 3 February 2026

disturbances can alter the surface roughness of the water, introducing components of surface scattering or Bragg scattering. Although water bodies generally exhibit low backscatter values across all four polarization modes, different polarizations vary in their sensitivity to surface roughness. Taking dual-polarized Sentinel-1 images as an example, under VV polarization, roughened water surfaces tend to show a more significant increase in backscatter compared to VH polarization. As shown in Fig. 2, some pixels in the central river area reach backscatter intensities of -13 dB, which are close to those of surrounding non-water areas. This can lead to a reduced extent of the identified water body.

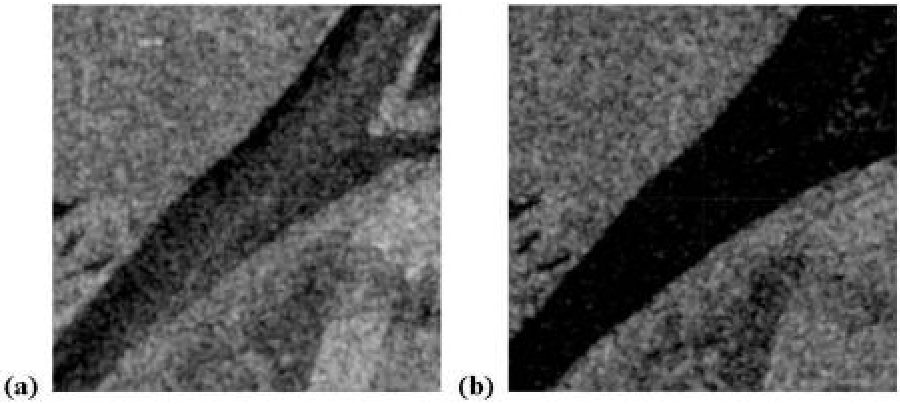

Figure 2: Comparison of different polarization images on the surface of roughened water bodies. (a) shows VV polarization image. (b) shows VH polarization image.

The backscatter from bare soil areas contains rich soil information, including soil moisture and soil texture. In arid desert regions, low soil moisture results in low internal charge polarization and a relatively small dielectric constant, allowing microwaves to easily penetrate the surface soil. In such cases, volume scattering is the dominant mechanism. As soil moisture increases, the dielectric constant also increases, and surface scattering becomes the dominant type. Different soil textures can also influence the dominant scattering mechanism—for example, fine-grained sand is more prone to volume scattering than blocky clay. Croplands are key areas of interest in flood monitoring. Compared to water bodies and bare soils, the backscatter coefficient in croplands shows distinct seasonal variations corresponding to crop growth stages.

Crop growth is generally divided into four stages: germination, vegetative, reproductive, and maturity. During the germination stage, crops are sparsely distributed, and the surface remains largely bare soil, resulting in backscatter characteristics similar to those of bare land. In the vegetative stage, crops grow rapidly. Increased stem height and higher leaf number and density lead to a sharp rise in the number of scattering elements, significantly enhancing volume scattering—particularly in VH polarization, where the backscatter coefficient increases notably. For VV polarization, the increase is less pronounced because crop stems are oriented nearly perpendicular to the ground, leading to a weaker response. During the reproductive and maturity stages, crop changes primarily involve fruit development, with little change in height or leaf number. The newly formed fruits serve as additional scattering elements, enhancing volume scattering. As a result, backscatter intensity continues to rise but remains relatively stable overall. By comparing three SAR images taken during different growth stages and the flood period, it is evident that there is a significant difference in backscatter intensity between the vegetative and maturity stages. As crops mature, backscatter intensity increases markedly. However, the intensity remains relatively stable between the vegetative stage and the flood period, making it more challenging to distinguish flooding from normal growth during that time.

4.1.2 Building areas

The scattering characteristics of urban (building) areas are highly complex and influenced by both imaging parameters (such as polarization mode, incidence angle, and resolution) and surface attributes (including building orientation, layout, and surface roughness). Densely arranged man-made structures can give rise to single, double, triple, or even multiple scattering events. As the number of scattering interactions increases, the signal's round-trip path length becomes longer, resulting in severe signal mixing among adjacent buildings. This poses significant challenges for interpreting SAR images in urban environments. Due to the large distance between spaceborne radar and ground targets, the incident radar beams can be approximated as parallel rays, simplifying certain aspects of geometric analysis but not mitigating the inherent complexity of urban backscatter.

The angle between building walls and the satellite's orbital direction can significantly influence the strength of double-bounce scattering. When the orbital direction is parallel to the building walls—meaning the radar beam plane is perpendicular to the wall surface—the double-bounce scattering is strongest. In this case, the echo generated by specular reflection lies in the same plane as the incident wave. When there is an angular offset between the orbital direction and the wall, the radar cross-section (RCS) energy is primarily composed of surface scattering, and the backscatter intensity decreases rapidly as the angle increases. In change detection or time-series analysis, it is essential to ensure that all images are acquired with the same orbit direction (either ascending or descending) to avoid significant changes in backscatter caused by orbital differences, which could reduce detection or analysis accuracy. During urban flooding, the land surrounding buildings becomes water-covered, leading to specular reflection as the dominant scattering type and a reduction in backscatter intensity. Assuming the building wall roughness remains unchanged, radar echoes are strengthened by energy reflected from the water surface onto the walls, resulting in a significant increase in backscatter intensity. Since the contributions from the sidewalls and rooftops remain largely unchanged, the transition zones between water and buildings may show a slight decrease in intensity, as seen in Fig. 3.

When other man-made structures are located near buildings, multiple scattering between sidewalls becomes complex and difficult to predict or model. Due to the increased round-trip path length, these effects are typically observed on the right side of the "bright line" region in the SAR image. Therefore, urban flooding tends to enhance backscatter intensity in building areas, but the magnitude of this enhancement is highly uncertain. Fig. 3 also illustrates changes in urban backscatter intensity following rainfall that occurred between July 19 and 22, 2021, with 24-hour precipitation totals of 103 mm, 380 mm, 398 mm, and 76 mm, respectively. The false-color composite image assigns the VV-polarized SAR images acquired on July 27, July 3, and June 21 to the RGB channels, respectively. In the image, blue-green areas represent open water bodies in natural regions, as the values in the Green and Blue channels are significantly higher than those in the Red channel. This suggests that the dominant scattering has shifted from volume scattering (typical of mature wheat fields) to specular reflection, indicating the crops were inundated by floodwaters.

Bright-colored areas with regular texture patterns indicate building regions. By comparing the building areas northwest and southeast of the river, the significant impact of flooding on backscatter intensity is evident. The southeastern urban area appears gray-white in the image, indicating that the backscatter intensity across the three acquisition dates is relatively consistent, with no significant change. In contrast, the northwestern urban area appears red, indicating a sharp increase in brightness in the Red channel—i.e., a significant rise in backscatter intensity during the flood period. This suggests severe urban flooding, which is further supported by the presence of extensive surrounding surface water.

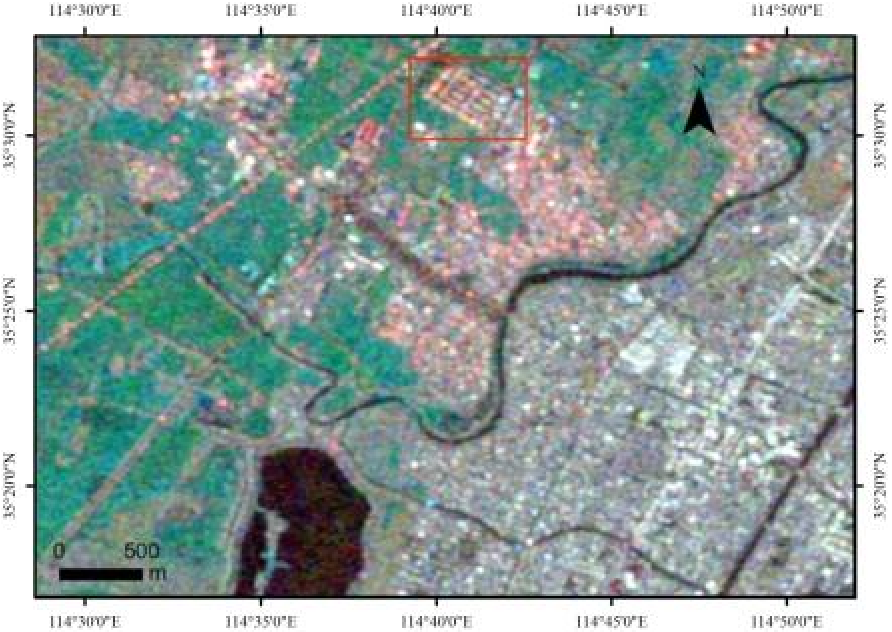

Figure 3: The influence of heavy rainfall on the strength of building areas. Imagery © 2022 NASA, Map data © 2022 Google

By closely examining the building area in the northwest, it is evident that the building structures, layout patterns, and densities vary significantly. For instance, the area outlined in red consists of uniformly arranged high-rise buildings, while most of the surrounding areas are densely packed with low-rise structures. Despite this variation, the region still appears predominantly red in the image, indicating that when standing water is present around buildings, the backscatter intensity increases significantly, regardless of whether the buildings are low-rise, mid-rise, or high-rise.

According to the rainfall data of GPM data, this trend becomes even more apparent in time-series SAR images, as shown in Fig. 4. In the absence of flooding, the VV-polarized backscatter intensity in urban areas ranges from -8.6 dB to -4.0 dB, while the VH-polarized intensity ranges from -13.7 dB to -9.8 dB, both exhibiting relatively stable fluctuations. This stability suggests that, compared to natural areas, building areas are less affected by seasonal variation, allowing for greater flexibility in time-series analyses without the need to constrain the images to the same season. This is particularly advantageous for studying changes and development trends in urban areas. Once flooding occurs, both VV and VH backscatter intensities increase sharply—by more than 6 dB—further indicating that changes in the roughness of surrounding surfaces disrupt the previously consistent backscatter signal of building areas. Therefore, using time-series SAR images to monitor urban flooding is both feasible and effective.

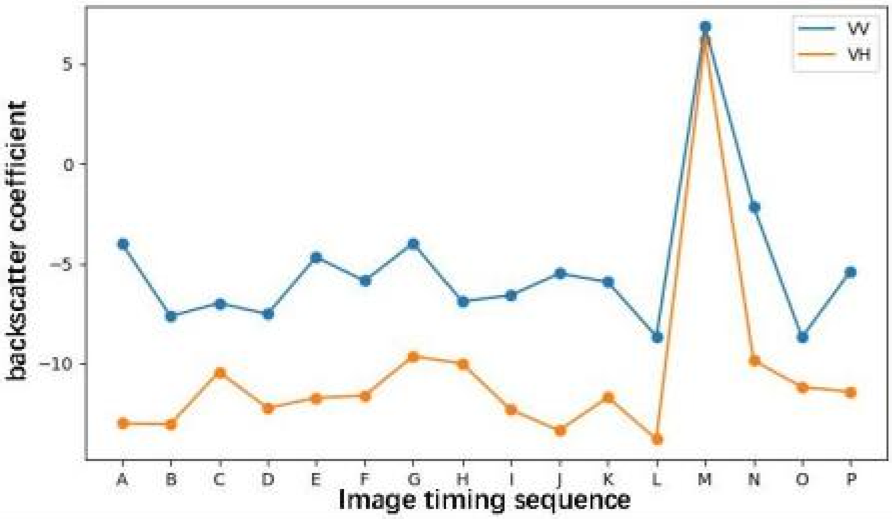

Figure 4: Trend of temporal SAR images (VV and VH polarization) in building areas within the red rectangular frame in Fig. 3.

4.2 Flood monitoring results and analysis in natural areas

When using the Z-score method for flood monitoring, it is necessary to set a threshold to distinguish between anomalous (flooded) and non-anomalous (non-flooded) pixels. However, unlike traditional thresholding methods, thresholds based on Z-scores have a clear statistical confidence level. To compare the accuracy of flood monitoring results under different confidence levels, this section defines three Z-score thresholds: -2, -2.5, and -3. According to the standard normal distribution table, these thresholds correspond to confidence levels of 95.4%, 98.8%, and 99.7%, respectively. The Z-score images generated using RRB images and the time-series SAR flood monitoring algorithm were clipped to match the coverage area of the validation images. The Z-score values were then classified using three thresholds, as shown in Fig. 5. It is important to note that seasonal water bodies were excluded during the accuracy assessment. This is because such water bodies consistently exhibit low backscatter intensity in time-series SAR images, whereas time-series monitoring primarily aims to highlight newly emerged surface water.

In Fig. 5, different colors are used to represent the flood monitoring results under different Z-score thresholds. As shown, lowering the confidence level introduces more speckled flood pixels but also captures more water bodies. For instance, noticeable pink pixels appear in the northern and eastern parts of Weihui under less strict thresholds, whereas using a threshold of -3 results in more missed detections in these areas. A comparison between Fig. 5a and 5b reveals a significant difference between the flood extent identified by Sentinel-2 on the 26th and that detected by SAR on the 27th, particularly in the floodplains upstream and downstream of the Wei River. These differences are also reflected in the accuracy assessment,

https://doi.org/10.5194/egusphere-2025-5770
Preprint. Discussion started: 3 February 2026

where the CSI and PA show discrepancies of up to 17% and 23%, respectively. The OA shows a slight increase, primarily because the flood and non-flood classes in Weihui are unevenly distributed, resulting in a high proportion of TN in the confusion matrix.

365 **Figure 5:** Comparison of monitoring results in the flood area of Weihui city based on the Z-score method. (a), 07/26/2021, (b), 07/27/2021, (c), 07/31/2021.

A comparison between the optical water extraction results from July 26 and July 31 reveals significant changes in the flood extent within Weihui City during this period. The flood areas in the upstream and midstream regions contracted, while the flooded areas in the downstream region expanded. As shown clearly in Fig. 6, the monitoring results from July 27 are highly consistent with the ground truth from July 31 in the downstream floodplain, whereas there is a notable difference when compared to the July 26 ground truth. This highlights the dynamic nature of flood disasters. When evaluating the accuracy of flood monitoring algorithms, it is crucial to consider both timeliness—the validation images should be as close in time as possible to the SAR acquisition—and sample size, using as much validation data as possible to ensure accurate and reliable assessment of the algorithm's performance. In the accuracy evaluations using the two Sentinel-2 scenes as ground truth, the proposed SAR-based flood monitoring algorithm achieved over 92% overall accuracy in both cases and showed strong consistency with the water extent derived from both the July 26 and July 31 ground truths. Overall, while lowering the confidence level introduced more speckled flood pixels, which led to a noticeable decline in UA, the CSI—which places greater emphasis on the correct identification of flood areas—increased to varying degrees. Therefore, a Z-score threshold of -2 can be considered appropriate for flood detection in natural areas. At the 95% confidence level, both study areas achieved approximately 90% OA and CSI values above 60%. In conclusion, the method proposed in this study demonstrated high accuracy within the study areas, indicating strong reliability and stability for flood monitoring applications.

Figure 6: Comparison of monitoring results in the downstream flood monitoring area of Weihui City based on the Sentinel-2 images. (a), 07/26/2021, (b), 07/27/2021, (c), 07/31/2021.

4.3 Flood monitoring results and analysis in building areas

In urban flood monitoring, it is also necessary to determine thresholds for identifying anomalies. This study found that the frequency distribution curves of Z-score images in building areas do not exhibit a bimodal pattern, indicating that the Otsu method (maximum inter-class variance) is not suitable for determining accurate thresholds in this context. Therefore, this section adopts the same confidence-level-based thresholds used for natural areas to monitor urban flooding, with threshold values set at 2, 2.5, and 3. In natural areas, using VV and VH polarizations from Sentinel-1 images helps mitigate interference from rough water surfaces, yielding better monitoring performance than single-polarization approaches. However, few studies have applied Sentinel-1 images for urban flood detection. Thus, this section first evaluates the performance of VV, VH, and dual-polarization combinations under the same threshold conditions in monitoring urban flooding.

The UAV images of Weihui City offer not only ultra-high spatial resolution and oblique viewing advantages, but also excellent timeliness. With an imaging time difference as short as 2 hours, it can be reasonably assumed that the flood extent remained largely unchanged during this interval. In this section, this validation dataset is used for a detailed analysis of the urban flood detection results based on time-series Sentinel-1 SAR images (Fig. 7). This study found that lower threshold values result in a significantly higher number of detected flood pixels compared to higher thresholds. In many areas, flood pixels identified at lower thresholds effectively filled the gaps and voids present in the higher-threshold results. Overall, the flood regions identified using lower thresholds exhibited better spatial continuity. Aside from a slight decline in UA, all other accuracy metrics showed improvements to varying degrees. Notably, the CSI—a key indicator of flood detection performance—achieved a 7.88% increase in accuracy.

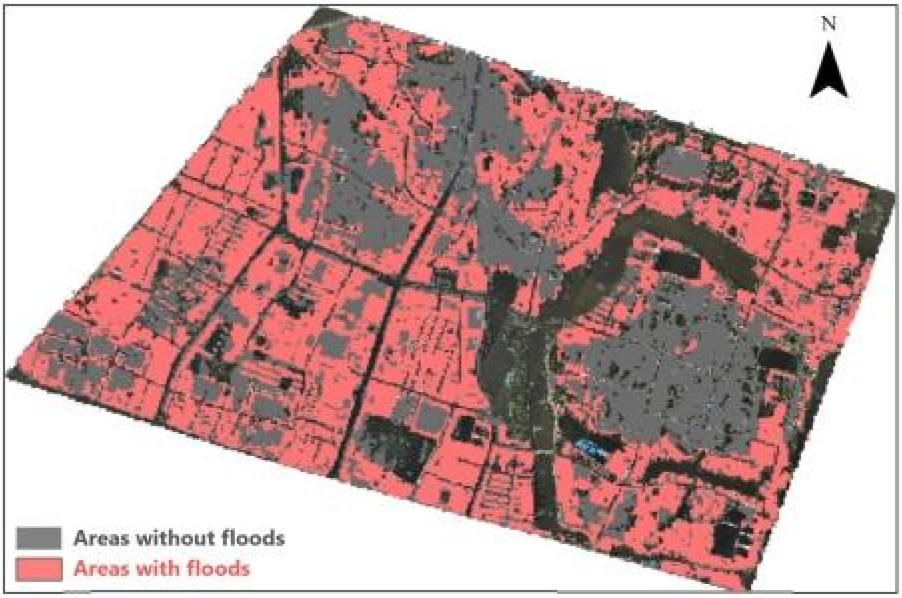

Figure 7: Flood monitoring results in the building area of Weihui city based on the Sentinel-1 images and Z-score. Grey indicates that the area has not been affected by the flood; red indicates that the area has been affected by the flood.

By comparing the identified flood regions with ground-truth data (Figure 8), it can be observed that in certain areas, the urban flood monitoring results differ significantly from the actual conditions. This section focuses on two typical regions for detailed analysis, where even with a relatively low threshold, the algorithm failed to effectively detect urban flooding. This suggests that in these areas, the backscatter intensity did not increase significantly. To better explain this phenomenon, relying solely on orthorectified images is insufficient. The UAV oblique views of the region, shown in Figures 8a and 8b, provide clearer insight. These images reveal that the area is low-lying, with most buildings being single-story or low-rise houses. The floodwaters in this region almost reach the rooftops of the buildings, meaning the dominant backscatter originates from the top surfaces of the structures and consists mainly of surface scattering, with little to no double-bounce scattering.

This highlights that the height difference between buildings and floodwaters is a critical factor influencing the accuracy of urban flood detection. From the perspective of side-looking radar, such buildings appear nearly as complete solid objects, with scattering dominated by rooftop reflections. In addition, narrow spacing between buildings can prevent the formation of double-bounce scattering, making it difficult to accurately identify floodwaters. In such cases, using SAR images with a smaller incidence angle may help improve detection accuracy, as it could increase the interaction between the radar signal and vertical structures, thus enhancing the detection of urban inundation.

Figure 8: UAV optical images when floods occurred in Weihui City. (a) represents areas severely inundated by floods; (b) represents areas with moderate flood inundation. Imagery © 2022 NASA, Map data © 2022 Google

5 Deficiencies and prospects

Time-series SAR images offer significant advantages in flood monitoring, and the method proposed in this study achieved high detection accuracy in both natural areas and urban areas. However, the full potential of time-series SAR data has not yet been fully realized, and several aspects warrant further research and refinement:

(1) Although forests and urban areas exhibit similar trends in backscatter intensity during flood events, this study did not address under-canopy flood detection due to a lack of validation data. Future research can explore this topic in depth, analyzing how factors such as phenological stages and precipitation events affect the consistency of backscatter intensity in forested regions. Based on this, a more robust under-canopy flood monitoring algorithm could be developed. Additionally, the proposed method also holds value for flood assessment in agricultural areas; for instance, in croplands with taller vegetation, more accurate estimates of flooded area may be achievable.

(2) In urban flood detection, the accuracy of the proposed method is influenced by building density and height differences. When buildings are densely packed or when the elevation difference between the building and water surface is small, double-bounce scattering becomes difficult to form, making intensity-based detection challenging. In future work, incorporating high-resolution DEM data could provide supplementary evidence by evaluating the height differences between flooded pixels and their neighbors, thereby improving urban inundation delineation.

(3) High-frequency flood monitoring can help generate more precise maps of flood-affected areas and provide timely support for disaster response. Since the proposed method allows for sensor-specific or configuration-specific adjustments by independently computing baseline statistics, it is feasible to incorporate multi-source time-series SAR images to increase the observation frequency during flood events. Furthermore, SAR images acquired at different wavelengths may offer additional insights for flood monitoring—for example, L-band SAR from satellites such as LuTan-1 may offer greater advantages in detecting under-canopy flooding.

6 Conclusions

Based on an analysis of the C-band SAR backscatter characteristics across different land cover types, this study proposes a novel method that integrates various auxiliary datasets to enable both large-scale flood monitoring and urban inundation detection. The main conclusions are as follows: By analyzing the scattering characteristics of time-series SAR images, it was found that in natural areas, vegetation growth status significantly affects intensity consistency, whereas in urban areas, rainfall-induced enhancement of double-bounce scattering can also disrupt intensity stability. Through the analysis of time-series backscatter intensity in urban regions, a Z-score-based flood classification tree was developed. The method calculates Z-score images using both reference and flood-period SAR images, enabling pixel-level flood probability estimation and assigning a clear statistical meaning to flood detection thresholds. The combination of VV and VH polarizations within the classification tree further enhances the reliability of flood identification. In the case of flood monitoring in Weihui City, the method demonstrated strong performance: the CSI and OA in natural areas reached 60% and 90%, respectively, while in urban areas, the CSI and OA reached 62% and 73%, respectively. The proposed method shows clear advantages in accurately classifying flood-affected areas and possesses the capability to simultaneously monitor widespread flooding and urban inundation. Therefore, it holds great potential for application in disaster prevention, mitigation, and emergency response.

Code and data availability. All codes used for the statistical analysis can be made available upon individual request. The database is available from the author upon reasonable request.

Author contributions. RX (study design, data curation, formal analysis, writing, reviewing). JZ (project lead, study design, data curation, writing, reviewing).

Competing interests. The contact author has declared that none of the authors has any competing interests.

References

Alvarez-Vanhard, E.; Corpetti, T.; Houet, T.: UAV & satellite synergies for optical remote sensing applications: A literature review. Science of remote sensing 2021, 3, 100019. DOI:10.1016/j.srs.2021.100019.

Amitrano, D.; Di Martino, G.; Di Simone, A.; Imperatore, P.: Flood detection with SAR: A review of techniques and datasets. Remote Sensing 2024, 16, 656.

Anusha, N.; Bharathi, B.: Flood detection and flood mapping using multi-temporal synthetic aperture radar and optical data. The Egyptian Journal of Remote Sensing and Space Science 2020, 23, 207-219. DOI:10.1016/j.ejrs.2019.01.001.

Barredo, J.I.: Major flood disasters in Europe: 1950–2005. Natural hazards 2007, 42, 125-148. DOI:10.1007/s11069-006-9065-2.

Borrelli, P.; Robinson, D.A.; Panagos, P.; Lugato, E.; Yang, J.E.; Alewell, C.; Wuepper, D.; Montanarella, L.; Ballabio, C.: Land use and climate change impacts on global soil erosion by water (2015-2070). Proceedings of the National Academy of Sciences 2020, 117, 21994-22001.

Cheadle, C.; Vawter, M.P.; Freed, W.J.; Becker, K.G.: Analysis of microarray data using Z score transformation. The Journal of molecular diagnostics 2003, 5, 73-81. DOI:10.1016/S1525-1578(10)60455-2.

Cian, F.; Marconcini, M.; Ceccato, P.; Giupponi, C.: Flood depth estimation by means of high-resolution SAR images and lidar data. Natural Hazards and Earth System Sciences 2018, 18, 3063-3084. DOI:10.5194/nhess-2018-158.

Clement, M.A.; Kilsby, C.G.; Moore, P.: Multi-temporal synthetic aperture radar flood mapping using change detection. Journal of Flood Risk Management 2018, 11, 152-168. DOI:10.1111/jfr3.12303.

Cruz, H.; Véstias, M.; Monteiro, J.; Neto, H.; Duarte, R.P.: A review of synthetic-aperture radar image formation algorithms and implementations: A computational perspective. Remote Sensing 2022, 14, 1258.

DeCarlo, L.T.: On the meaning and use of kurtosis. Psychological methods 1997, 2, 292.

DeVries, B.; Huang, C.; Armston, J.; Huang, W.; Jones, J.W.; Lang, M.W.: Rapid and robust monitoring of flood events using Sentinel-1 and Landsat data on the Google Earth Engine. Remote sensing of Environment 2020, 240, 111664. DOI:10.1016/j.rse.2020.111664.

Doane, D.P.; Seward, L.E.: Measuring skewness: a forgotten statistic? Journal of statistics education 2011, 19. DOI:10.1080/10691898.2011.11889611.

Du, W.; Xia, Q.; Cheng, B.; Xu, L.; Chen, Z.; Zhang, X.; Huang, M.; Chen, N.: Flood Inundation Probability Estimation by Integrating Physical and Social Sensing Data: Case Study of 2021 Heavy Rainfall in Henan, China. Remote Sensing 2024, 16, 2734.

Fernandez, P.; Mourato, S.; Moreira, M.; Pereira, L.: A new approach for computing a flood vulnerability index using cluster analysis. Physics and Chemistry of the Earth, Parts a/b/c 2016, 94, 47-55. DOI:10.1016/J.PCE.2016.04.003.

Geudtner, D.; Torres, R.; Snoeij, P.; Davidson, M.; Rommen, B.: Sentinel-1 system capabilities and applications. In Proceedings of the 2014 IEEE geoscience and remote sensing symposium, 2014; pp. 1457-1460. DOI:10.1109/IGARSS.2014.6946711.

Groeneveld, R.A.; Meeden, G.: Measuring skewness and kurtosis. Journal of the Royal Statistical Society Series D: The Statistician 1984, 33, 391-399.

Jongman, B.; Ward, P.J.; Aerts, J.C.: Global exposure to river and coastal flooding: Long term trends and changes. Global Environmental Change 2012, 22, 823-835. DOI:10.1016/j.gloenvcha.2012.07.004.

Kang, W.; Xiang, Y.; Wang, F.; Wan, L.; You, H.: Flood detection in Gaofen-3 SAR images via fully convolutional networks. Sensors 2018, 18, 2915. DOI:10.3390/s18092915.

Kummerow, C.; Simpson, J.; Thiele, O.; Barnes, W.; Chang, A.; Stocker, E.; Adler, R.; Hou, A.; Kakar, R.; Wentz, F.: The status of the Tropical Rainfall Measuring Mission (TRMM) after two years in orbit. Journal of applied meteorology 2000, 39, 1965-1982. DOI:10.1175/1520-0450(2001)040<1965:TSOTTR>2.0.CO;2.

Kunkel, K.E.: North American trends in extreme precipitation. Natural hazards 2003, 29, 291-305. DOI:10.1023/A:1023694115864.

Li, H.; Zhao, J.; Yan, B.; Yue, L.; Wang, L.: Global DEMs vary from one to another: an evaluation of newly released Copernicus, NASA and AW3D30 DEM on selected terrains of China using ICESat-2 altimetry data. International Journal of Digital Earth 2022, 15, 1149-1168. DOI:10.1080/17538947.2022.2094002.

Liu, B.; Li, Y.; Zhang, Y.; Wu, Z.; Pan, Y.; Li, M.: Multi-criteria decision-making method for emergency shelter site selection considering flood risk: A case study of Zhuhai, China. Cleaner Engineering and Technology 2025, 24, 100892. DOI:10.1016/j.clet.2025.100892.

Liu, X.; Huang, Y.; Xu, X.; Li, X.; Li, X.; Ciais, P.; Lin, P.; Gong, K.; Ziegler, A.D.; Chen, A.: High-spatiotemporal-resolution mapping of global urban change from 1985 to 2015. Nature Sustainability 2020, 3, 564-570. DOI:10.1038/s41893-020-0521-x.

Martinis, S.; Kuenzer, C.; Wendleder, A.; Huth, J.; Twele, A.; Roth, A.; Dech, S.: Comparing four operational SAR-based water and flood detection approaches. International Journal of Remote Sensing 2015, 36, 3519-3543. DOI:10.1080/01431161.2015.1060647.

Martinis, S.; Plank, S.; Ćwik, K.: The use of Sentinel-1 time-series data to improve flood monitoring in arid areas. Remote Sensing 2018, 10, 583.

Moreira, A.; Prats-Iraola, P.; Younis, M.; Krieger, G.; Hajnsek, I.; Papathanassiou, K.P.: A tutorial on synthetic aperture radar. IEEE Geoscience and remote sensing magazine 2013, 1, 6-43. DOI:10.1109/MGRS.2013.2248301.

Nhangumbe, M.; Nascetti, A.; Ban, Y.: Multi-temporal Sentinel-1 SAR and Sentinel-2 MSI data for flood mapping and damage assessment in Mozambique. ISPRS International Journal of Geo-Information 2023, 12, 53.

Pekel, J.-F.; Cottam, A.; Gorelick, N.; Belward, A.S.: High-resolution mapping of global surface water and its long-term changes. Nature 2016, 540, 418-422. DOI:10.1038/nature20584.

Tang, G.; Clark, M.P.; Papalexiou, S.M.; Ma, Z.; Hong, Y.: Have satellite precipitation products improved over last two decades? A comprehensive comparison of GPM IMERG with nine satellite and reanalysis datasets. Remote sensing of environment 2020, 240, 111697. DOI:10.1016/j.rse.2020.111697.

Tellman, B.; Sullivan, J.A.; Kuhn, C.; Kettner, A.J.; Doyle, C.S.; Brakenridge, G.R.; Erickson, T.A.; Slayback, D.A.: Satellite imaging reveals increased proportion of population exposed to floods. Nature 2021, 596, 80-86. DOI:10.1038/s41586-021-03695-w.

Tingsanchali, T.: Urban flood disaster management. Procedia engineering 2012, 32, 25-37. DOI:10.1016/j.proeng.2012.01.1233.

Torres, R.; Snoeij, P.; Geudtner, D.; Bibby, D.; Davidson, M.; Attema, E.; Potin, P.; Rommen, B.; Floury, N.; Brown, M.: GMES Sentinel-1 mission. Remote sensing of environment 2012, 120, 9-24.

Tripathi, G.; Pandey, A.C.; Parida, B.R.; Kumar, A.: Flood inundation mapping and impact assessment using multi-temporal optical and SAR satellite data: a case study of 2017 Flood in Darbhanga district, Bihar, India. Water Resources Management 2020, 34, 1871-1892. DOI:10.1007/s11269-020-02534-3.

Twele, A.; Cao, W.; Plank, S.; Martinis, S.: Sentinel-1-based flood mapping: a fully automated processing chain. International Journal of Remote Sensing 2016, 37, 2990-3004. DOI:10.1080/01431161.2016.1192304.

Voigt, S.; Giulio-Tonolo, F.; Lyons, J.; Kučera, J.; Jones, B.; Schneiderhan, T.; Platzeck, G.; Kaku, K.; Hazarika, M.K.; Czaran, L.: Global trends in satellite-based emergency mapping. Science 2016, 353, 247-252. DOI:10.1126/science.aad8728.

Voigt, S.; Martinis, S.; Zwenzner, H.; Hahmann, T.; Twele, A.; Schneiderhan, T.: Extraction of flood masks using satellite based very high resolution SAR data for flood management and modeling. In Proceedings of the RIMAX Contributions at the 4th International Symposium on Flood Defence (ISFD4), 2009. DOI:10.1007/s00403-001-0286-7.

Wang, T.; Tong, C.: An analytical model of double scattering for SAR imaging of urban structures. Optik 2018, 171, 484-491. DOI:10.1016/j.ijleo.2018.06.084.

Wang, Z.; Qin, Y.; Zhang, Q.; Li, Y.; Liu, J.; Yuan, X.; Zhao, L.; Li, M.; Cao, S.: China's GaoFen-3 Mission: A review. IEEE Geoscience and Remote Sensing Magazine 2025.

Xu, H.: Modification of normalised difference water index (NDWI) to enhance open water features in remotely sensed imagery. International journal of remote sensing 2006, 27, 3025-3033. DOI:10.1080/01431160600589179.

Zhang, J.; Zhou, C.; Xu, K.; Watanabe, M.: Flood disaster monitoring and evaluation in China. Global Environmental Change Part B: Environmental Hazards 2002, 4, 33-43. DOI:10.3763/ehaz.2002.0404.

Zhang, M.; Liu, D.; Wang, S.; Xiang, H.; Zhang, W.: Multisource remote sensing data-based flood monitoring and crop damage assessment: A case study on the 20 July 2021 extraordinary rainfall event in Henan, China. Remote Sensing 2022, 14, 5771.

Zhao, J.; Pelich, R.; Hostache, R.; Matgen, P.; Wagner, W.; Chini, M.: A large-scale 2005–2012 flood map record derived from ENVISAT-ASAR data: United Kingdom as a test case. Remote Sensing of Environment 2021, 256, 112338. DOI:10.1016/j.rse.2021.112338.

Zhao, L.; Zhang, Q.; Li, Y.; Qi, Y.; Yuan, X.; Liu, J.; Li, H.: China's Gaofen-3 satellite system and its application and prospect. IEEE Journal of Selected Topics in Applied Earth Observations and Remote Sensing 2021, 14, 11019-11028. DOI:10.1109/JSTARS.2021.3122304.